Interfacial Kinetics Induced Phase Separation Enhancing Low-Temperature Performance of Lithium-Ion Batteries

Kaikai Li [a, b, †], Dongmei Lin [b, †], He Huang [c, †], Dongqing Liu [d], Baohua Li [d], San-Qiang Shi [b], Feiyu Kang [d], Tong-Yi Zhang [a, e, *], and Limin Zhou [b, *]

[a] School of Materials Science and Engineering, Harbin Institute of Technology, Shenzhen, China

[b] Department of Mechanical Engineering, The Hong Kong Polytechnic University, Hong Kong, China

[c] Department of Mechanical and Aerospace Engineering, The Hong Kong University of Science and Technology, Clear Water Bay, Kowloon, Hong Kong, China

[d] National Local Joint Engineering Laboratory of Carbon Functional Materials, Graduate School at Shenzhen, Tsinghua University, Shenzhen 518055, P.R. China

[e] Materials Genome Institute, Shanghai University, 333 Nanchen Road, Shanghai 200444, China

* Corresponding author information:

E-mail: mmlmzhou@polyu.edu.hk (Limin Zhou)

E-mail: mezhangt@ust.hk (Tong-Yi Zhang)

† These authors are equal main contributors.

1

Abstract

Understanding the temperature dependence of phase transitions occurred in electrode materials is crucial for improving the low-temperature performance of Li-ion batteries. In this work, we find an unusual temperature dependence in the phase transition of TiO_2 nanoparticles on dynamic Li^+ intercalation, with a decrease in temperature resulting in the formation of a supersaturated solid solution phase. Kinetic analyses reveal that Li redistribution is facilitated at high temperature while limited at low temperature. This difference manifests as a thermodynamically-controlled phase separation at high temperature and a kinetically-controlled formation of a supersaturated solid solution phase at low temperature. Facilitating the phase separation by enhancing the interfacial kinetics proves effective to improve the low-temperature performance. This study provides a comprehensive and in-depth understanding of the temperature dependence of the lithiation-induced phase transition, which has important implications for the development of the next generation of all-climate rechargeable batteries.

Keywords: phase transitions, interfacial kinetics, lithiation, temperature dependence, Raman spectroscopy, supersaturated solid solution phase

1. Introduction

Rechargeable Li-ion batteries (LIBs) are widely used in digital devices, electric vehicles, stationary energy storage wells, and the aerospace industry [1-4]. In addition to the requirements of a high energy density and extended life cycles, LIBs must provide a stable output and rapid charge/discharge capabilities over a wide range of temperatures, especially when powering electric vehicles or hybrid electric vehicles [5-7]. The application of LIBs is

severely restricted, however, because they often experience significant capacity loss at low temperatures [5,8-11]. Studies of the failure mechanism at extended temperature ranges have generally suggested that a decrease in Li-ion transport kinetics in both electrolytes and active materials is responsible for capacity deterioration at low temperatures [10,12-15]. One study of the electrochemical properties of layered Li-rich oxides at 25 °C and 0 °C also suggested that the lattice contractions caused by a decrease in temperature may be responsible for the capacity loss [16]. Another study found that reducing the particle size of the $LiFePO_4/C$ electrode can improve its performance at low temperatures [17]. These findings indicate that the temperature influences the electrochemical performances of LIBs by changing the physical characteristics of the electrode materials. The nature of the electrode material directly determines its phase/structure evolution during the charging/discharging process, a process upon which electrochemical performance is highly dependent [18,19]. However, phase transitions of electrode materials at extended temperature ranges remain poorly understood, due in part to difficulties associated with the direct monitoring of the electrode system in its operating environments. Thus, few studies have investigated temperature-dependent phase transitions during electrochemical (de)lithiation. Meethong et al. examined the effects of temperature on the miscibility gap between Li_xFePO_4 and $Li_{1-y}FePO_4$ phases and found that the miscibility gap in $LiFePO_4$ contracted systematically as temperature increased [20]. Delacourt et al. found experimental evidence for a temperature-driven solid solution phase of Li_xFePO_4 ($0 \leq x \leq 1$) at 450 °C despite the well documented two-phase nature of Li_xFePO_4 at room temperature [21]. In contrast, Mai et al. revealed the formation of intermediate solid solution phases between $LiFePO_4$ and $FePO_4$ during lithiation/delithiation at low temperatures, and proposed that the formation of the intermediate phases was due to the reduced Li ion diffusion coefficient in Li_xFePO_4 which resulted in accumulation of overpotential at the phase boundary of $LiFePO_4/FePO_4$ and strong polarization at low temperatures [22]. They further investigated the

3

phase transition of $Na_3V_2(PO_4)_3$ at various temperatures and demonstrated that during desodiation the phase evolution process was a one-phase solid solution reaction, rather than a traditional two-phase transition, at low temperatures, and found that the diffusion coefficients of Na ion in $Na_3V_2(PO_4)_3$ decreased by reducing the temperature [23]. Interestingly, both high and low temperatures can induce the formation of the intermediate solid solution phase. Notwithstanding these pioneering studies, understanding of the fundamentals of the dependence on temperature of lithiation-induced phase transition, which is critical for the design of all-climate rechargeable batteries, still remains seriously limited.

In this study, we aim to address this limited understanding by examining the phase transition of anatase TiO_2 upon Li^+ ion intercalation across a range of different temperatures. Anatase TiO_2 shows promise as an intercalation-type LIB electrode because of its low volume expansion upon lithiation, fast charging capability and potentially high capacity when cycling between 0.01–3V [7,24], and is an ideal model electrode for this research. Operando Raman spectroscopy reveals an unusual temperature dependence in the phase transition of anatase TiO_2 nanoparticles on dynamic Li^+ intercalation, with a decrease in temperature resulting in the formation of a supersaturated solid solution phase. Thermodynamic analyses show that increasing temperature narrows the two-phase miscibility gap, which is contrary to the observed temperature dependence. Kinetic analyses illustrate that Li redistribution is facilitated at high temperature but limited at low temperature as a result of the sluggish Li transportation across the electrolyte-electrode interface. This difference is seen to manifest as the particle-to-particle phase separation at high temperature and the formation of a supersaturated solid solution phase at low temperature. Enhancing interfacial kinetics and creating an interconnected electrode architecture proves to be an effective means of weakening the temperature dependence, facilitating phase separation, and improving low-temperature performance of LIBs. Our findings provide, for the first time, a uniquely comprehensive and in-depth explanation for the

4

temperature dependence of lithiation-induced phase transitions, which can be used to understand the phase transitions at various temperatures of other electrode materials.

2. Results and Discussion

2.1. Operando Raman spectroscopy for phase identification

Operando Raman spectroscopy was developed to characterize the phase transition of anatase TiO$_2$ nanoparticles during electrochemical (de)lithiation at various temperatures. Anatase TiO$_2$ has a tetragonal crystal structure (α phase), which is transformed into an orthorhombic structure (β phase) via lithium intercalation (Fig. 1a) [25]. Through comparative analyses between operando XRD and operando Raman spectra, we demonstrated that, in the case of TiO$_2$, the Raman spectra information was sufficient and effective for phase identification during (de)lithiation, as shown in Figs. S1-S4. By tracing the evolution of the E_g peak at ~144 cm^{-1} of TiO$_2$ (α(E_g)) and the B_{2g} peak at ~163 cm^{-1} of Li$_x$TiO$_2$ (β(B_{2g})), phase transition during (de)lithiation was monitored as a function of time. Fig. 1b clearly shows the evolution of the α(E_g) peak and the β(B_{2g}) peak during discharge/charge cycling. The gradual disappearance(appearance) of the α(E_g) peak and the appearance(disappearance) of the β(B_{2g}) peak correspond to the phase transition. With Li$^+$ insertion, the α(E_g) peak of the anatase phase shifted to higher frequencies (Fig. 1c-d). A linear relationship can be assumed between the Raman shift of α(E_g) peak and the Li concentration (Fig. 1d). If there are certain peaks with Raman shifts which are higher than that of α(E_g) but lower than that of β(B_{2g}), it then indicates the existence of phases with Raman shifts that deviate from those of α and β phases, and these phases are named as the supersaturated solid solution phase in current study (Fig. 1d), which is characterized by the intensity in Raman spectrum between the α(E_g) and β(B_{2g}) peaks (Fig. S4). The supersaturated solid solution phase is such a phase that the Li concentration in this phase

5

When discharge potential reaches the plateau region, the coexistence of two peaks reflects the coexistence of two phases. Further lithiation resulted in the disappearance of the $\alpha(E_g)$ peak, so that only the $\beta(B_{2g})$ peak could be found, indicating that the α phase was completely transformed into the β phase. During Li$^+$ extraction, reverse spectra evolution was observed, which indicated the reversible phase transition from the β phase to the α phase.
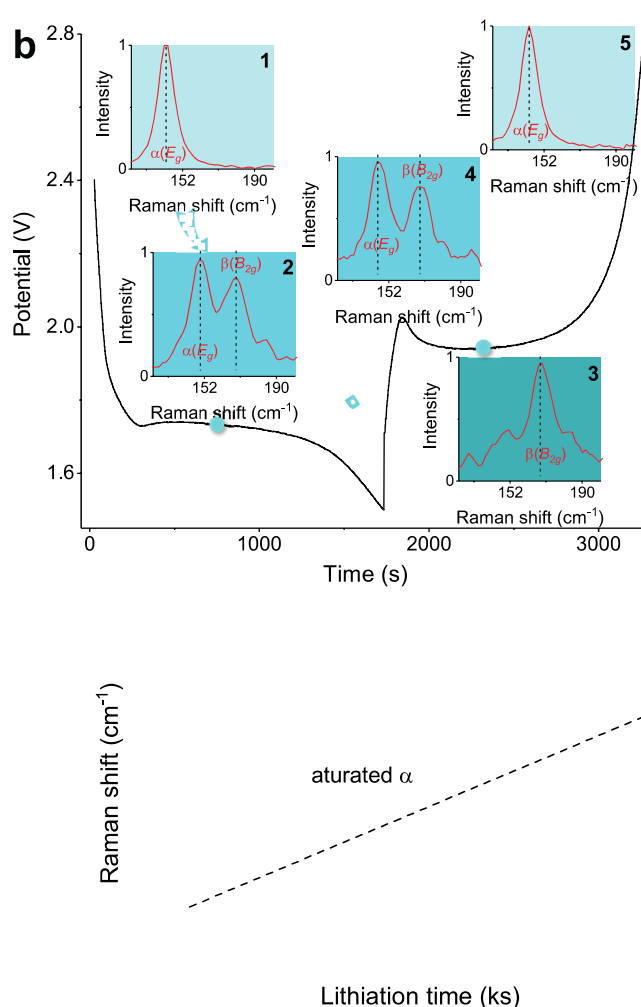
Fig. 1. Crystal structure and Raman spectra of TiO$_2$ during lithiation. (a) Crystal structures of TiO$_2$ and Li$_{0.5}$TiO$_2$. (b) Operando Raman spectroscopic monitoring of the phase transition of TiO$_2$ during lithiation and delithiation. (c) The evolution of the Raman peak at $\sim$ 144 cm^{-1} with

6

Li concentration. (d) The Raman peak positions of α phase, β phase and the supersaturated solid solution phase during 1C lithiation.

## 2.2. Temperature dependence of lithiation-induced phase transitions

In general, the (de)lithiation transition of bulk TiO_2 proceeds through a nucleation and growth process with a fixed thermodynamic miscibility gap. The transition was reflected in the operando Raman spectra as the diminishment of the α(E_g) peak and the enhancement of the β(B_{2g}) peak, or vice versa. Meanwhile, a distinct gap with very low intensity should be identified between the peaks, as illustrated in Fig. S5c. Fig. 2a-c and Fig. S7 show the two-dimensional intensity mapping of the operando Raman spectra of TiO_2 nanoparticles during 1C discharging/charging at 0 °C, 25 °C, and 40 °C respectively. Fig. 2a-c detail the evolution of the α(E_g) and β(B_{2g}) peaks. At all temperatures, it was found that the intensity distribution between the α(E_g) peak and the β(B_{2g}) peak during lithiation was greater than the background intensity. The emergence of the greater intensity distribution between the two peaks indicated the formation of phases or structures that differed from both the α phase and the β phase, which was not caused by the possible pseudo-capacitive effects while the Li ions would be stored on the surface region of the nanoparticles, because there was no intensity distribution with Raman shifts higher than that of the α phase in the initial stage of discharge. Previous studies have repeatedly demonstrated that a higher discharging current density will result in the appearance of an intensity distribution between two correlative X-ray diffraction peaks of two endmember phases of $LiFePO_4$, and this intensity distribution represents the formation of the supersaturated solid solution phase [26-29]. Further comparison of the operando Raman spectra of the TiO_2 nanoparticles lithiated at 1C and 0.1C (Fig. S8) at 25 °C revealed that the intensity distribution between the α(E_g) peak and the β(B_{2g}) peak at 1C was higher than at 0.1C. We can thus attribute

the intensity distribution between the two Raman peaks to the formation of a supersaturated solid solution phase. When the TiO_2 nanoparticles were lithiated at 1C and 40 °C, as shown in Fig. 2c, the intensity distribution between the $\alpha(E_g)$ and $\beta(B_{2g})$ peaks was weaker than the distribution observed when lithiation occurred at 1C and 25 °C. However, when the temperature was decreased to 0 °C (Fig. 2a), a stronger intensity distribution was observed between the two peaks during lithiation, indicating that a decrease in temperature favors the formation of the supersaturated solid solution phase during lithiation of TiO_2 nanoparticles. This phenomenon contrasts sharply with the well-established knowledge that an increase in temperature results in an increase in the solid solution limit and thus favors the formation of the solid solution phase at higher temperatures.

Analysis of the individual Raman spectra collected during cell operation revealed more evidence of these phenomena. Fig. 2d shows an obvious intensity band between the two peaks in the selected Raman spectra. Furthermore, a decrease in temperature was seen to enhance the intensity band. Fig. 2e shows the peak-fitting of a selected Raman spectrum collected at 0 °C using a Gauss-Lorentz profile. As can be clearly seen, the peak-fitting is good only if an additional peak (phase) is taken into consideration, and the additional peak is derived from the supersaturated solid solution phase. Without consideration of this additional phase, as shown in Fig. S9, the experimental spectrum and the fitted spectrum display distinct differences. By fitting the Raman spectra with α and β two-phase coexistence, it is found that the supersaturated phase can be identified in all the spectra, as shown in Fig. 1d. Besides, the evolution of the full width at half maximum (FWHM) and the mole fraction of the supersaturated phase exhibits similar trend (Fig. S10), that they first increased and then decreased with time. This trend also demonstrated that the intensity distribution between the $\alpha(E_g)$ and $\beta(B_{2g})$ peaks was not caused by the possible pseudo-capacitive effects. The non-constant FWHM, especially the very large ones (e.g., > 20 cm^{-1}), indicates that the supersaturated phases should have various Li

concentrations (the fitted Raman peak belonging to the supersaturated phase should be composed of several peaks of smaller FWHM), which is in line with previous observation of the continuous solid solution phases in LiFePO$_4$ by XRD measurements [26]. Fig. S11 shows the peak position evolution of the $\alpha(E_g)$ and $\beta(B_{2g})$ peaks during 1C lithiation-delithiation at various temperatures. A decrease in temperature shifted the peak positions of both phases to higher frequencies during lithiation, and the difference between the peak positions of the two phases ($\Delta_{Raman\ shift}$) was nearly constant across a range of temperatures. Therefore, the emergence of the intensity distribution between the two peaks is therefore not induced by a decrease in $\Delta_{Raman\ shift}$. In contrast to the lithiation process, the delithiation transition was seen to seemingly independent of temperature, as shown in Fig. 2a-d. The intensity distribution between the $\alpha(E_g)$ and $\beta(B_{2g})$ peaks during delithiation was nearly the same at various temperatures, and no difference could be seen between the peak positions (Fig. S11). This finding implies that the lithiation and delithiation transitions of TiO$_2$ are asymmetrical and probably differ in their reaction mechanism. A similar asymmetry between lithiation and delithiation has also been observed in LiFePO$_4$ [26, 30], and could be attributed to spatial heterogeneities in reaction rates, which are amplified during delithiation, but suppressed during lithiation [30]. To clarify the underlying mechanisms of the distinct and unusual temperature dependence of the phase transition during dynamic Li$^+$ intercalation, systematic thermodynamic and kinetic analyses were conducted.
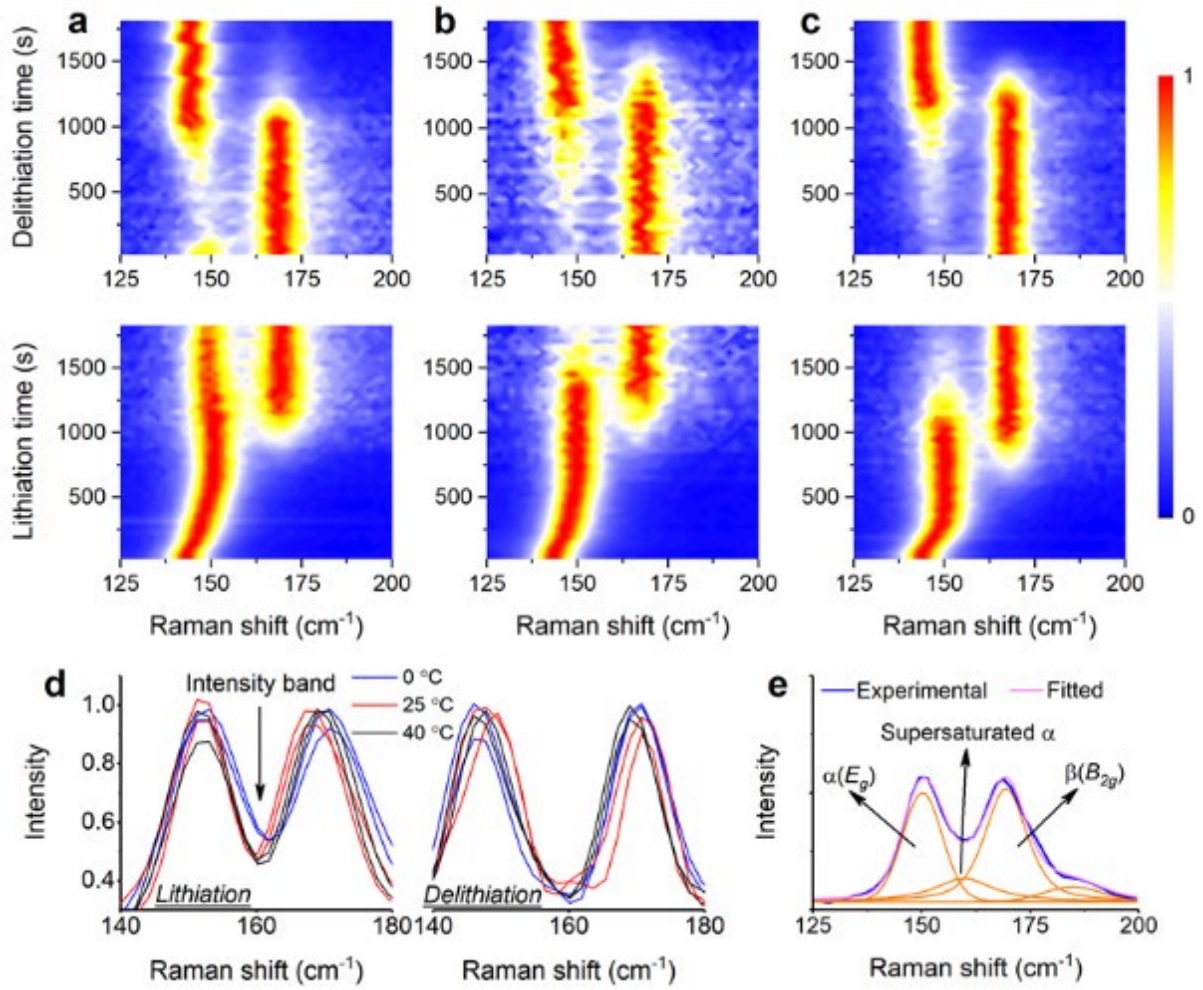
Fig. 2. Operando Raman spectroscopy. (a-c) Two-dimensional normalized intensity mapping of operando Raman spectroscopy of TiO$_2$ nanoparticles during 1C lithiation-delithiation at (a) 0 °C, (b) 25 °C, and (c) 40 °C. The spectra intensities were normalized to their individual maximum of each spectrum. (d) Comparison of selected Raman spectra at various temperatures. (e) Fitting of the selected Raman spectrum at 0 °C, with consideration of the supersaturated solid solution phase.

2.3. Thermodynamics during lithiation at different temperatures

To reveal the thermodynamics of the lithiation of TiO$_2$ nanoparticles, Raman spectra of a lithiated TiO$_2$ electrode at equilibrium were collected via a mapping function at various

temperatures. Based on the mapping results (Fig. S12), the selected area's phase constitution distribution was determined by I_α/I_β (where I_α is the intensity of the $\alpha(E_g)$ peak and I_β is the intensity of the $\beta(B_{2g})$ peak in a single Raman spectrum), as shown in Fig. 3a-c. The average value of I_α/I_β in the selected area at 25 °C, 0 °C and −10 °C is 0.93, 0.98 and 0.99, respectively, which indicates that the volume fraction of β phase slightly decreased and volume fraction of α phase slightly increased as temperature decreases. This is also reflected in the color change in Fig. 3a-c. The evolution of the intensity ratio I_α/I_β implies that the Li concentration limit in β phase may increase in order to maintain a constant global Li concentration. To determine the Li concentration limits in α phase and β phase at various temperatures, the peak positions of the Raman spectra were analyzed. The Raman shift distributions of the α and β phases at various temperatures are plotted in Fig. 3d-f and Fig. 3g-i, respectively. The Raman shift of the α phase decreased as the temperature decreased, indicating that a decrease in temperature decreases the Li concentration limit of the α phase. Meanwhile, the Raman shift of the β phase increased as the temperature decreased, indicating that the Li concentration limit of the β phase increases at low temperatures. Based on the Raman mapping results at various temperatures, we established the phase diagram for the Li-TiO$_2$ system (Fig. 3j). We use the average value of the Raman shifts of the α phase or β phase in the selected area (Table S1) to represent the theoretical Raman shifts of the α phase or β phase when the two phases are in equilibrium at a certain temperature. The phase diagram shows that these results are consistent with the established knowledge that the solid solubility will be increased and the miscibility gap will be narrowed at higher temperatures. The lithiation thermodynamics of TiO$_2$ was further analyzed using a galvanostatic intermittent titration technique (GITT). The equilibrium potential (E_{eq}) during lithiation of TiO$_2$ nanoparticles is shown in Fig. S13. We assumed isotropic physical properties, and that the chemical free energy density $f_V(X)$ of a particle can be modeled using regular solution formulation (Note S3). The chemical free energy density $f_V(X)$ was then plotted as a

11

function of the mole filling fraction X of a regular solution of Li atoms and available vacancies on the TiO$_2$ lattice, as shown in Fig. 3k. The mole filling fraction X_1 and X_2 at the two minima in the free energy curve correspond to the solid solution limit in the α phase and the solute concentration limit in β phase, respectively, and the difference between X_1 and X_2 is the two-phase miscibility gap at equilibrium. Raising the temperature slightly narrowed the two-phase miscibility gap, which is consistent with the phase diagram shown in Fig. 3j.
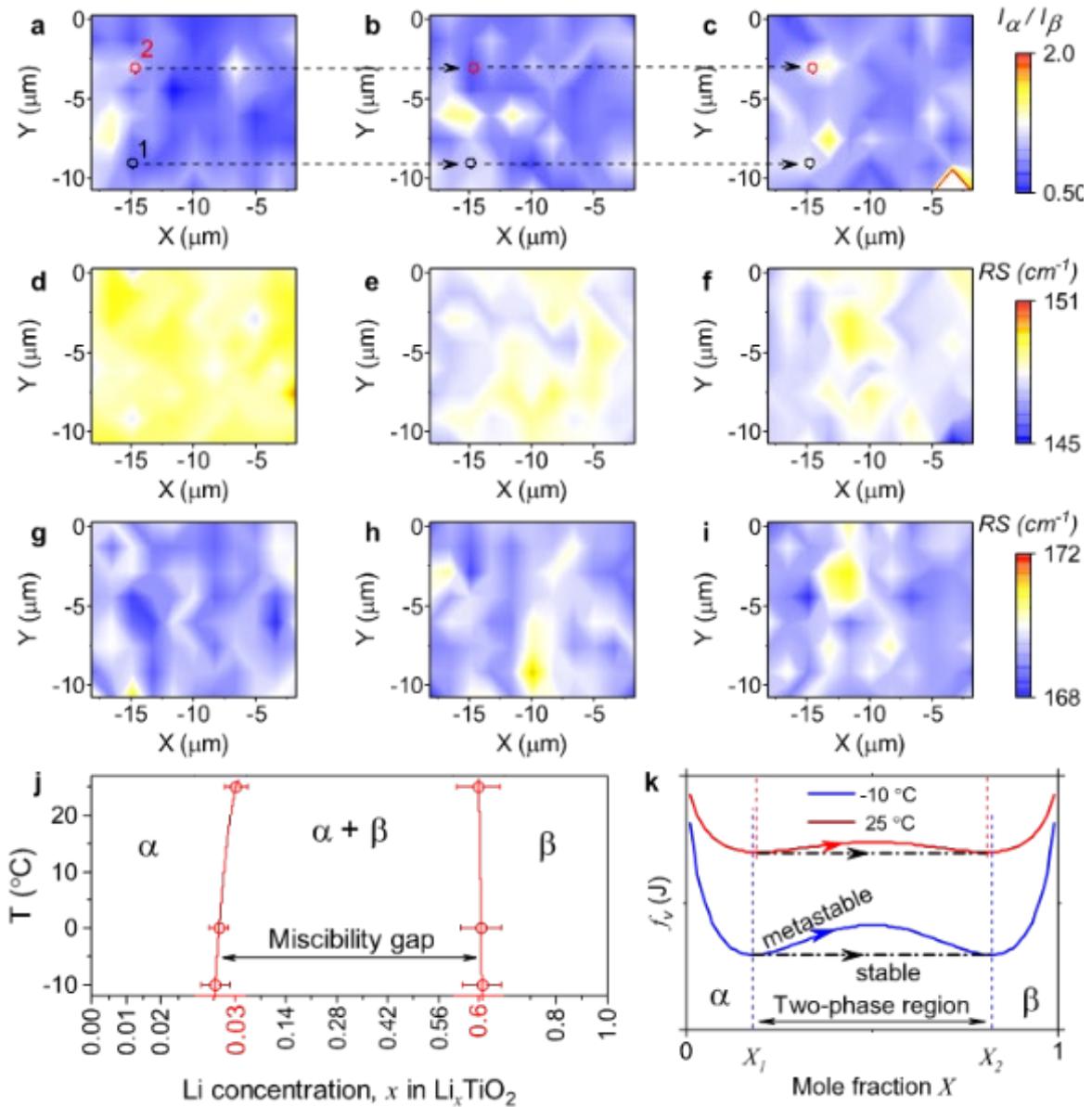

Fig. 3. Raman mapping of lithiated TiO$_2$ nanoparticle electrode at equilibrium state. (a-c) Phase constitution distribution at (a) 25 °C, (b) 0 °C, and (c) −10 °C. (d-f) Raman shift (RS) of the α

phase at various positions at (d) 25 °C, (e) 0 °C, and (f) −10 °C. (g-i) Raman shift of the β phase at various positions at (g) 25 °C, (h) 0 °C, and (i) −10 °C. (j) Phase diagram of Li-TiO$_2$ system obtained from Raman mapping results. The Li concentration in the α and β phases at 25 °C were set to 0.03 and 0.6 according to the literature [31]. (k) Free energy versus mole filling fraction X of a regular solution of Li atoms and available vacancies on TiO$_2$ lattice at different temperatures.

Ab-initio molecular dynamic (MD) simulations were also conducted to elucidate the influence of temperature on the lithiated TiO$_2$ in thermodynamic equilibrium. A simulated Li$_n$Ti$_{16}$O$_{32}$ supercell was relaxed with n values ranging from 1 to 10. Fig. 4a shows the lattice constant changes for Li$_6$Ti$_{16}$O$_{32}$ ($x = 0.375$ in Li$_x$TiO$_2$) over time at 260 K, 300 K and 800 K, respectively. The relaxation of the Li$_n$Ti$_{16}$O$_{32}$ supercell can be treated as the spinodal decomposition of a supersaturated solid solution phase (Fig. 4b). Generally, the supersaturated phase will separate to an α phase and a β phase after relaxation. When the temperature was set to 260 K or 300 K, phase separation occurs. However, when temperature was 800 K, the structure of Li$_{0.375}$TiO$_2$ unceasingly changed between phase separation and supersaturated solid solution phase, implying that the phase separation could be suppressed at 800 K or above. The average lattice constants after relaxation are plotted in Fig. 4c-d. The difference between lattice constants a and b decreased with an increase in temperature, suggesting that the relaxed structure at high temperature was closer to the crystal structure of the α phase ($a = b$). XRD measurements were further conducted on a lithiated TiO$_2$ nanoparticle electrode (with two-phase coexistence and Li concentration being 0.258) under various temperatures, as shown in Fig. 4e. The XRD patterns at 173 K and 300 K show that the electrode had two phases. When the temperature was raised from 173 K to 800 K, three peaks corresponding to the β phase

disappeared and the remaining two β phase peaks at ~44.2° and ~51.6° gradually shifted to lower angles. The XRD pattern at 800 K was first indexed by using the Winplotr software and then fitted with the XFIT software to obtain the peak profile. Finally, the Chekcell program was used to conduct the space group assignment. The above analysis suggested the formation of a new intermediate phase, and the new phase crystallized in the tetragonal system and may have a space group of I41acd (Fig. 4e) or P42nnm (Fig. S17). Precise determination of the crystal structure of the new phase requires more comprehensive and accurate measurements and calculations. Nevertheless, it can be reasonably assumed that the new intermediate phase formed at high temperatures has a crystal structure closer to the room-temperature α phase (crystal system: tetragonal. Space group: I41amd), rather than the β phase (crystal system: orthorhombic. Space group: Imma) [25]. In light of this, the *ab-initio* MD simulation and XRD results indicate that increasing temperature should favor the formation of the solid solution phase. Thus, it can be concluded that the influence of temperature on the equilibrium thermodynamics was not the reason for the formation of the supersaturated solid solution phase during the lithiation transition of the TiO_2 nanoparticles.

On the other hand, it was observed that the time cost for phase separation at 260 K is longer than at 300 K (Fig. 4a). This implies that once the supersaturated solid solution phase was formed, it was relatively more stable at low rather than high temperatures. This observation is consistent with the changes in free energy obtained at different temperatures using GITT (Fig. 3k). We can see that the phase transition at −10 °C was more prone to go through a metastable route instead of a stable phase separation route than at 25 °C, which is similar to the supersaturation model proposed by Mai et al. to illustrate the phase transition mechanism of $FePO_4$ to $LiFePO_4$ at different temperatures [22]. To continuously explore the inherent mechanism of the formation of the supersaturated solid solution phase, we then examine the influence of temperature on the kinetics during the dynamic lithiation of the TiO_2 nanoparticles.
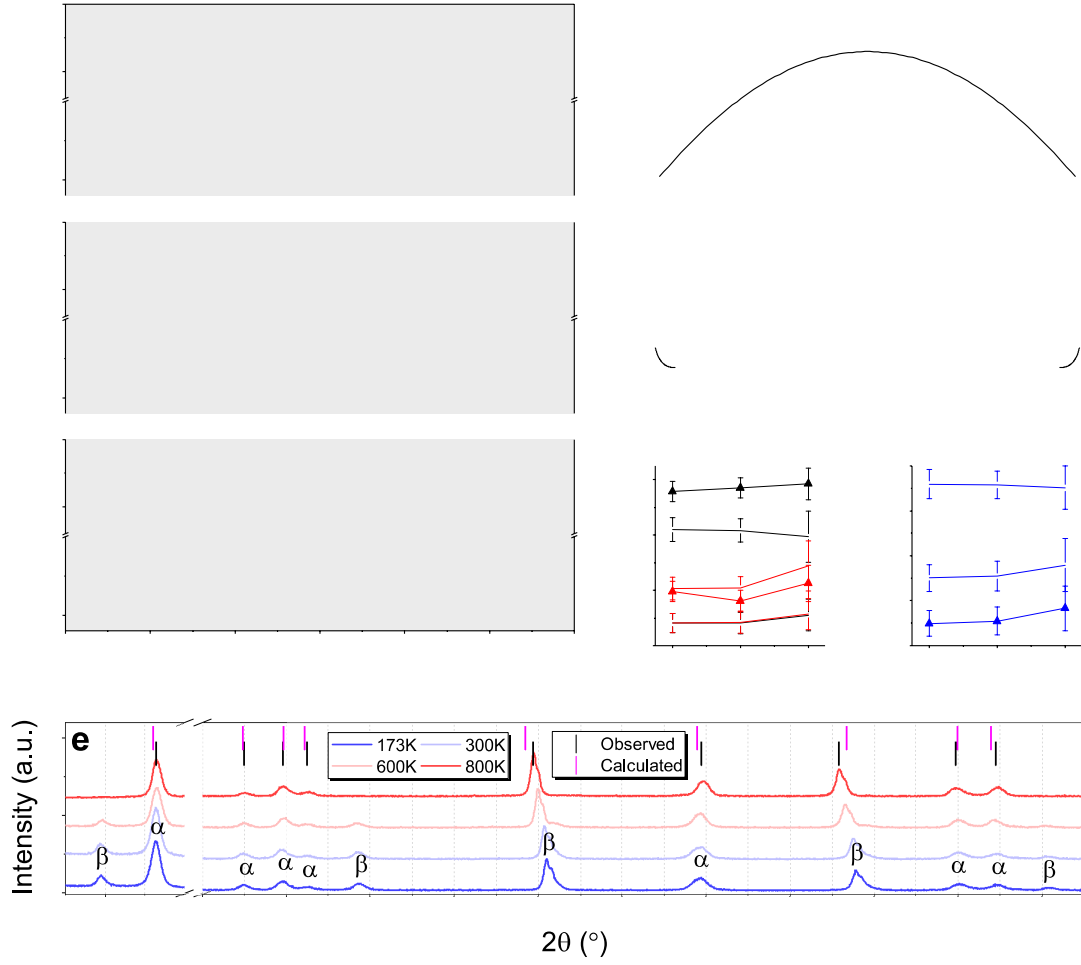
Fig. 4. *Ab-initio* MD simulations and XRD measurements. (a) Lattice constant (*a, b, c*) changes of $Li_{0.375}TiO_2$ during the *ab-initio* MD simulation at different temperatures. (b) Illustration of the phase diagram and Gibbs free energy as a function of Li concentration at a given temperature T_1. (c) The average lattice constants *a, b* of the Li_xTiO_2 structure over the 4-6 ps simulations at different temperatures (●: *a* of $Li_{0.0625}TiO_2$, ●: *b* of $Li_{0.0625}TiO_2$, ■: *a* of $Li_{0.375}TiO_2$, ■: *b* of $Li_{0.375}TiO_2$, ▲: *a* of $Li_{0.5}TiO_2$, ▲: *b* of $Li_{0.5}TiO_2$). (d) The average lattice constant *c* of the Li_xTiO_2 structure after 4 ps simulation at different temperatures (●: *c* of $Li_{0.0625}TiO_2$, ■: *c* of $Li_{0.375}TiO_2$, ▲: *c* of $Li_{0.5}TiO_2$). (e) The XRD patterns of lithiated TiO_2 nanoparticles collected at various temperatures. The black and purple vertical bars mark the observed peak positions and calculated peak positions based on I41acd space group for the XRD pattern measured at 800 K, respectively.

15

2.4. Kinetics during dynamic lithiation at different temperatures

It is worthy of note that the evolution of the Raman intensity ratio (I_α/I_β) shown in Fig. 3a-c is not synchronous at various sites of the electrode (e.g., site 1 and site 2 in Fig. 3a). A similar phenomenon was observed during the galvanostatic discharging of the TiO_2 nanoparticle electrodes. It was expected that the TiO_2 electrode would constantly transform from the α phase to the β phase during the lithiation process due to the constantly increasing Li concentration. Interestingly, however, the reverse transition was observed during the lithiation process of the TiO_2 nanoparticle electrodes, as indicated by the marked rectangular region in Fig. 5a. Additionally, the Raman spectra shown in Fig. 2a indicate that the α phase still remained at the end of the lithiation process. The survived α phase gradually disappeared during the delithiation by absorbing more lithium ions on the initial delithiation, which was possible because the thermodynamic equilibrium state with the overall Li content, at the end of the lithiation process or at the beginning of the delithiation process, should be in the β phase. The supersaturated solid solution phase or the particles of β phase with higher Li concentration would be the possible Li sources for these particles of the survived α phase. These phenomena reflect the Li redistribution within the electrode, and we propose that the phenomena are caused by the inter-exchange of Li^+ between different particles.

To demonstrate this hypothesis, we conducted EIS measurements with a TiO_2 nanoparticle electrode discharged for 0.5 h at a current density of 1C without relaxation at different temperatures. The results are shown in Fig. 5b-c. Unlike the EIS spectra collected at open circuit potential (OCP) before discharging (Fig. S18), the inclined straight line disappeared, and obvious inductive loops appeared in the spectra at higher temperatures. Fitting the EIS spectrum using the model proposed in Fig. S19 further confirmed the existence of inductance. Inductance

16

is defined as the propensity of an electrical conductor to produce a reverse electromotive force that opposes a change in the current flowing through the circuit [32]. Two mechanisms – adsorption/desorption of Li^+ and interparticle Li^+ transportation – were ever reported accounting for the inductive loop in EIS spectra [32,33-37]. The adsorption/desorption mechanism implies that the appearance of the inductive loop should be independent of the Li concentration. However, our results (Fig. S18b) showed that there was no inductive loop when the cell was discharged for only 10 min. Thus, the inductive loop, resulted from the generation of an electromotive force superimposed upon the Li^+ intercalation during discharging, could be attributed only to the interparticle Li transportation generating a field that opposes the field caused by the global electrochemical discharging [32,37]. This will result in such a scenario that, although the global Li concentration of the electrode increases constantly during discharging, the Li concentration of certain particles may decrease while that of others will increase due to the interparticle Li transportation, causing the Li redistribution in the electrode. The SECM (Fig. 5d-f) images show that the surface conductivity of the electrode decreased nonuniformly at different positions during lithiation, which further indicates a redistribution of Li within the electrode.

In the many-particle electrode (Fig. 5g), different particles will reach slightly different depth of discharge (DOD) during Li^+ intercalation due to physical or structural heterogeneities (e.g., difference in electronic conductivity and particle size) [38]. Under this condition, simulations and experiments have shown that because of the small particle size, phase separation will occur between different nanoparticles rather than within a single nanoparticle at a constant temperature like room temperature [38-43]. Nanoparticles with higher DOD within the spinodal region have a larger driving force to be lithiated, while others tend to be delithiated [38]. As a result, the TiO_2 nanoparticles reach either an almost fully lithiated β phase or an almost fully delithiated α phase, which is illustrated in the high temperature route in Fig. 5g. Instead of the

constant lithiation of each single particle, Li redistribution occurs as a result of thermodynamic relaxation and dominates the dynamics of the phase separation [38]. Therefore, the operando Raman spectra of the TiO_2 nanoparticle electrode during lithiation collected at high temperatures (Fig. 2b-c) exhibit more distinct two-phase character.

Fig. 5b-c show that the inductive loops are more obvious at high temperature. Meanwhile, the frequency where the inductive loops appear decreases at lower temperature. This means that raising temperature can enhance the interparticle Li transportation (Li redistribution), while decreasing temperature makes the interparticle Li transportation very sluggish so that Li redistribution was limited at low temperature like 0 °C [32]. The sluggish interparticle Li transportation at 0 °C result from the deceleration of the Li diffusion across the electrolyte-electrode interface. This is evidenced by the significantly enlarged charge transfer resistance with temperature decreasing from 40 °C to 0 °C (Fig. 5b), which is also consistent with the change of the overpotential with temperature. As marked in Fig. 5b, the voltage decreased to 0.93V after discharging for 0.5h at 0 °C, much lower than at 25 °C and 40 °C. Fig. S22 also shows that the discharging voltage profile at −10 °C deviates more from the equilibrium potential profile than that at 25 °C. The decrease in temperature significantly retarded the Li diffusion across the electrolyte-electrode interface, making the interparticle Li transportation extremely difficult. Thereby, we concluded that the formation of supersaturated solid solution phase at low temperature originates from the limited Li redistribution as a result of the sluggish interparticle Li transportation. In this condition, the particle-to-particle phase separation is suppressed [38], and the constant lithiation prevails in a single particle [26-28,44-46]. This results in the emergence of much higher intensity distribution between the $\alpha(E_g)$ and $\beta(B_{2g})$ peaks at lower temperature (0 °C in Fig. 2). Meanwhile, the sluggish Li diffusion kinetics and suppression of phase separation resulted in the degradation of the electrochemical performance at low temperatures.
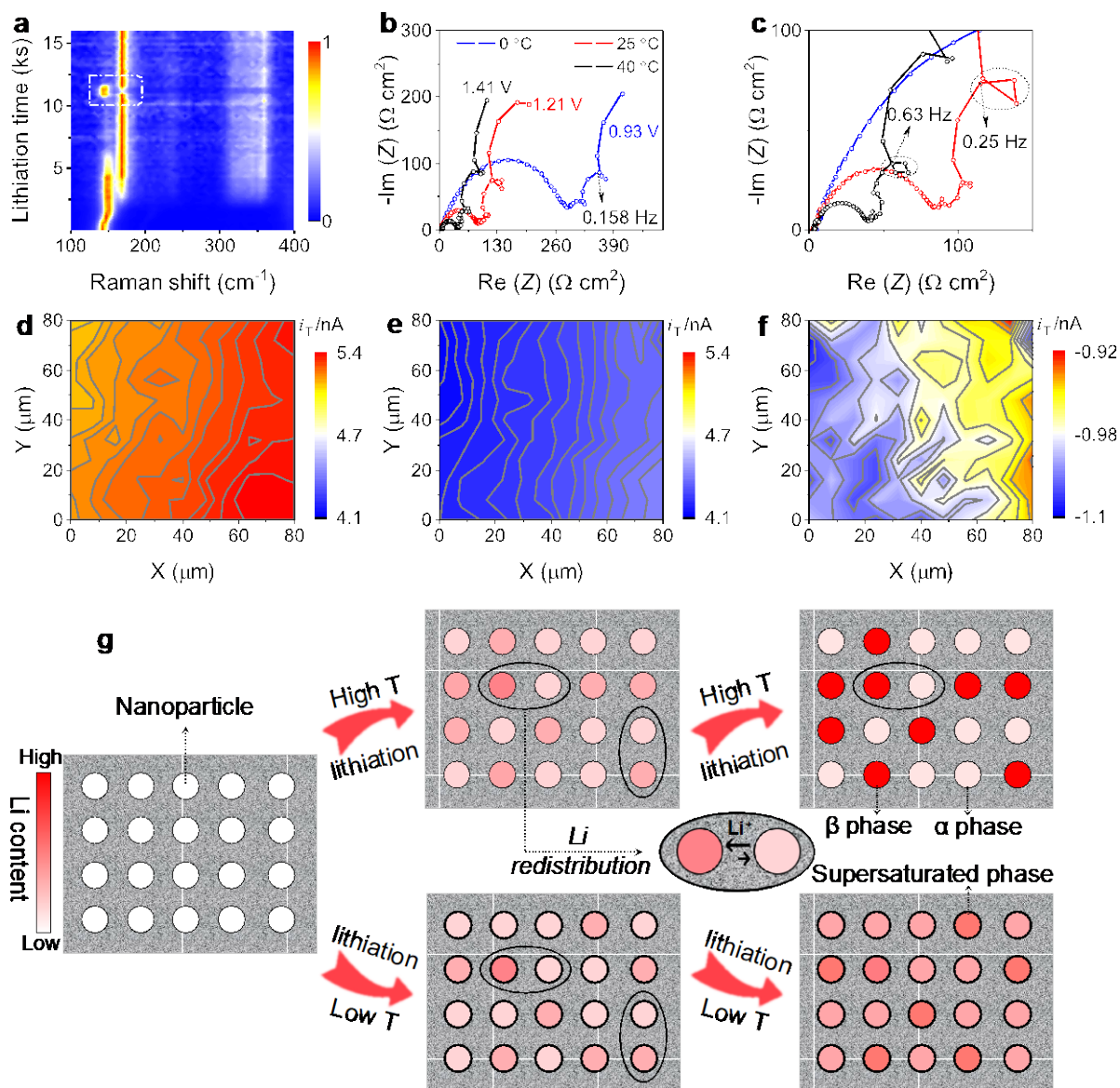
Fig. 5. Li redistribution and particle-to-particle phase separation. (a) Two-dimensional normalized intensity mapping of the operando Raman of TiO_2 nanoparticles during 0.1C lithiation at 25 °C. (b) EIS spectra collected after the cell assembled using TiO_2 nanoparticles was discharged at a current density of 1C for 0.5 h at various temperatures. (c) Enlarged view of (b). (d-e) *In situ* SECM mapping of the TiO_2 nanoparticle electrode (d) before discharging at open circuit potential (OCP) and (e) after discharging to 1.5V. (f) The decrement of the tip current (i_T) after discharging from OCP to 1.5V. (g) Schematic illustration of lithiation of nanoparticles in the electrode at various temperatures.

2.5. Kinetic approach to improve low-temperature performance

Our results reveal that the Li redistribution is boosted at high temperature but suppressed at low temperature as a result of the sluggish Li^+ transportation across the electrolyte-electrode interface, which is the origin of the temperature dependence of the phase transitions and formation of supersaturated solid solution phase at low temperatures. This crucial finding inspires us that the enhancement of low-temperature performance of LIBs can come from promoting Li transportation across the electrolyte-electrode interface and Li interexchange among the active materials to facilitate the phase separations. Following the protocols described above, here we transformed the TiO_2 nanoparticles into TiO_2 nanowires (Fig. S20) and compared their performance at 25 °C and −10 °C (Fig. 6). The nanoparticles and nanowires were both composed of anatase phase (Fig. S21) and exhibited typical discharge/charge potential profiles for anatase TiO_2 anodes at 25 °C and −10 °C (Fig. S22). Significantly, the capacity of the nanowire anode at −10 °C reached 64% of its capacity at 25 °C, doubling the value for the nanoparticle anode. When the temperature was elevated from −10 °C to 25 °C, the nanowire anode regained its original high capacity and exhibited excellent battery performance for a wider temperature range. Fig. 6a compares the R_{ct} and $E_{a,ct}$ of the nanowire anode and the nanoparticle anode. The R_{ct} of the nanowire anode was significantly lower than that of the nanoparticle anode at all temperatures, while the $E_{a,ct}$ of the nanowire anode was around 20 meV lower than that of the nanoparticle anode. This means that Li transportation across the electrolyte-electrode interface was significantly enhanced by the nanowire anode, reducing the overpotentials for lithiation. The enhanced interfacial kinetics are expected to weaken the temperature dependence of the phase transitions during lithiation and boost the Li redistribution (i.e., facilitate the phase separation), which are evidenced by the operando Raman and EIS

results. Fig. 6c-d show the operando Raman spectra of the TiO_2 nanowires during 1C discharging/charging at 40 °C and 0 °C. The intensity distribution between the $\alpha(E_g)$ and $\beta(B_{2g})$ peaks during both lithiation and delithiation appeared to be nearly the same at different temperatures. Fig. 6e shows obvious inductive loops in the EIS spectra of the TiO_2 nanowire anode at both 40 °C and 0 °C after discharging, which contrasts with the straight lines observed at OCP (Fig. S24) and is more prominent than those observed for nanoparticle anode (Fig. 5b-c). Furthermore, the inductive loop appeared at the same frequency at different temperatures, indicating the same degree of difficulty for the Li redistribution. From the morphological and structural points of view, the nanowires may form a three-dimensional interconnected porous network through wire-to-wire connection which boosts the Li redistribution among the nanowires [47,48]. In comparison with the nanoparticles, the nanowires might provide faster electron or/and ion transfer channels, thereby lowering the charge transfer resistance. These experimental findings suggest that optimizing the multi-particle kinetics involved in the electrolyte-electrode interface and designing the electrode architecture are important for improving the low temperature performance of LIBs.
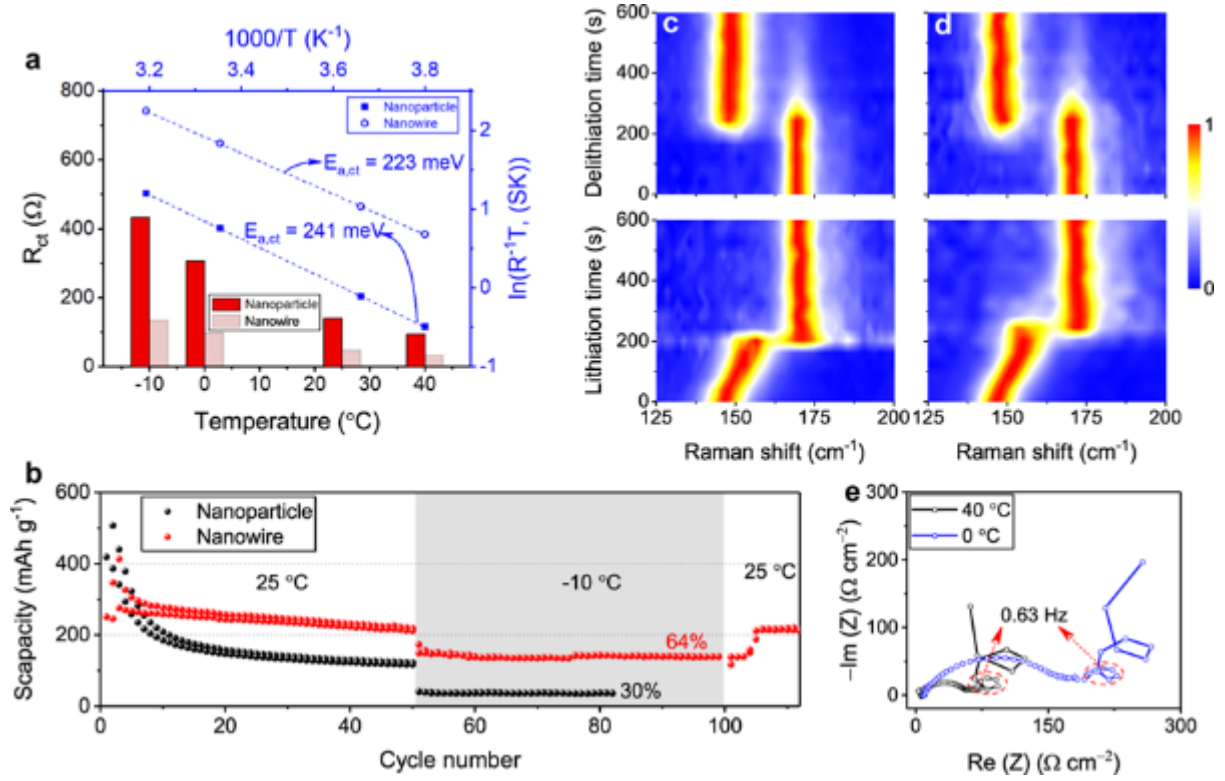
Fig. 6. Lithiation of TiO$_2$ nanowires. (a) R$_{ct}$ of the nanoparticle electrode and nanowire electrode at various temperatures and corresponding charge transfer energy barrier E$_{a, ct}$. (b) Comparison of the electrochemical performance of nanoparticle electrode and nanowire electrode at 25 °C and −10 °C at a current density of 0.1C. (c-d) Two-dimensional normalized intensity mapping of the operando Raman spectra of TiO$_2$ nanowires during 1C lithiation-delithiation at (c) 40 °C and (d) 0 °C. (e) EIS spectra collected after the cell assembled using TiO$_2$ nanowires was discharged at a current density of 1C for 0.5 h without relaxation at different temperatures.

3. Conclusion

In this study, we provide a comprehensive and in-depth interpretation for the unusual temperature dependence of lithiation-induced phase transition using TiO$_2$ electrode as a model. We first revealed that the phase transition of TiO$_2$ nanoparticles during dynamic Li$^+$

intercalation was clearly dependent on temperature and a supersaturated solid solution phase formed at low temperatures, which seemingly runs contrary to the traditional understanding of thermodynamics. Afterwards, thermodynamic analyses showed that, despite the narrowing of the two-phase miscibility gap that results from an increase in temperature, the supersaturated solid solution phase was relatively more stable at low temperatures. Further kinetic analyses demonstrated that Li interparticle exchange causing Li redistribution in the electrode facilitated the particle-to-particle phase separation at high temperatures, however, at low temperatures, the particle-to-particle phase separation tended to be suppressed because of the sluggish Li diffusion kinetics across the electrolyte-electrode interface. Therefore, the constant lithiation dominated in each nanoparticle, which kinetically induced the formation of the supersaturated solid solution phase at low temperatures. Boosting Li transportation in the electrolyte-electrode interface and creating interconnected active material architecture proved to be an effective means to weaken the temperature dependence of lithiation-induced phase transitions, facilitate the phase separation, and improve the low-temperature performance of LIBs. Our findings will have important implications for the development of the next generation of all-climate rechargeable batteries.

4. Experimental section

4.1. Operando Raman spectroscopy

For preparation of the working electrode, TiO_2 was mixed mechanically with super P. A 5 wt% solution of Polytetrafluoroethylene (PTFE) was then added and mixed until a homogenous slurry was obtained. The final mass ratio of TiO_2, super P, and PTFE was 8:1:1. After drying, the slurry was rolled into a thin film and then pressed onto a stainless-steel mesh that acted as the current collector. A delicate airtight electrochemical cell with a quartz window on the

positive case was designed and used for operando Raman spectroscopy. The cell was assembled in an argon-filled glove box ($O_2 \leq 0.5$ ppm, $H_2O \leq 0.5$ ppm) with lithium metal foil as the counter-electrode. A 1 M solution of $LiPF_6$ in a mixture of ethylene carbonate (EC) and diethyl carbonate (DEC) (1:1 = v/v) was used as the electrolyte. Celgard 2400 film was used as a separator. The cell was cycled for 3 times at 1C prior to the operando Raman measurements. The operando Raman measurements were conducted at 40 °C and 1C, followed by measurements at 25 °C and 0 °C, respectively, using the same cell.

The Raman spectra were recorded at various temperatures using a MicroRaman system (LabRAM HR spectrometer, Horiba) with an Olympus BX microscope. The spectra were excited with an argon ion laser (532.05 nm). Each spectrum required a measurement time of 20 s, with two repeated accumulations. The Raman spectra were continuously collected as the operando Raman cell was (dis)charged in a galvanostatic mode under a constant current density of 1C or 0.1C (1C = 335 mA g^{-1}). Raman mapping acquisition was conducted at 25 °C, 0 °C, and −10 °C. Before Raman mapping acquisition at 25 °C, the cell was discharged at 0.1C for 6 h and then relaxed for 12 h. Subsequently, the cell temperature was decreased to 0 °C, and the cell was relaxed for 2.5 h followed by Raman mapping acquisition. This procedure was repeated at −10 °C. The cell temperature was controlled in a temperature-controlled chamber (Linkam Scientific) using a nitrogen-gas flow and electronic heaters (Linkam Scientific) for temperature-dependent experiments.

4.2. Electrochemical measurement

For preparation of the electrodes, TiO_2 (70 wt.%), carbon black (20 wt.%), and poly(vinylidene fluoride) (PVDF, 10 wt.%) were mixed in N-methylpyrrolidone (NMP). The obtained homogenous slurry was pasted on a Cu foil and dried in a vacuum oven at 110 °C for 12 h. Coin cells were assembled in an argon-filled glove box ($O_2 \leq 0.5$ ppm, $H_2O \leq 0.5$ ppm)

with lithium metal foil as the counter electrode, and 1 M $LiPF_6$ solution in a mixture of ethylene carbonate and diethyl carbonate (1:1 = v/v) was used as the electrolyte. Celgard 2400 film was used as a separator. The mass loading of TiO_2 in the electrodes was ~ 1.5 mg cm^{-2}. All EIS measurements were carried out using a PARSTAT 4000 electrochemical workstation. A frequency range of 10^5 Hz to 100 mHz and an AC voltage amplitude of 10 mV was chosen. The cell temperature was controlled in a temperature-controlled chamber (Linkam Scientific) and was varied between 0 °C and 40 °C (±0.1 °C) using a nitrogen-gas flow and electronic heaters (Linkam Scientific) for temperature-dependent experiments. Galvanostatic discharging/charging (GDC) and galvanostatic intermittent titration technique (GITT) tests were conducted on a Landt battery tester at different temperatures. Typically, GITT measurements consisting of a series of current pulses were applied to the coin cell at a current density of 0.5C for 3 min, each followed by a 150 min relaxation period. The voltage window of GITT measurement was 1.6 V to 2.2 V. Prior to the GITT measurement, the cell was galvanostatic cycled at 0.5C for 5 cycles between 1.6 V to 3 V.

4.3. Ab-initio molecular dynamic (MD) simulations

All density functional theory (DFT) calculations were carried out under the generalized gradient approximation with the Perdew–Burke–Ernzerhof functionals [49,50] as implemented in the Vienna *ab-initio* simulation package [51]. *Ab-initio* molecular dynamic simulations [52] were carried out in a $2 \times 2 \times 1$ supercell of $Li_nTi_{16}O_{32}$ (n = 1, 2, 4, 6, 8 and 10) anatase phase at 260 K, 300 K and 800 K, with a timestep of 2 fs to observe the phase transition to the lithium titanate phase. Pressure was constantly maintained at 1 atm using the variable cell approach [53]. The Parrinello-Rahman (NPT) scheme was used with a Langevin thermostat as implemented in VASP [54]. For the detailed setting of the Langevin dynamics, the friction coefficient is set to be 10 ps^{-1} for both the atomic degrees-of-freedom and the lattice degrees-

of-freedom. All degrees of freedom were allowed to change, including lattice constants and angles between lattice vectors. The simulation supercell and large kinetic cutoff of 520 eV made the computations extremely expensive, therefore systems were only simulated for 10 ps to observe the phase transition process with different lithium concentrations and temperatures. The atomic trajectories of selected $Li_nTi_{16}O_{32}$ supercells were displayed with the collection of the last 2000 simulation steps using Visual Molecular Dynamics (VMD) [55] software. The dynamic lattice constants were traced during the whole simulation to distinguish the phase evolution. The lattice parameters of a = b = 7.58 Å and c = 9.50 Å of the pristine α phase were initially set in all AIMD simulations of Li_xTiO_2 with different Li concentrations and the dynamic and equilibrium lattice constants were traced during the lattice relaxation processes at temperatures of 260 K, 300 K, and 800 K in order to investigate the phase evolution.

4.4. Temperature-resolved XRD measurements

For the preparation of the electrode, the TiO_2 nanoparticles were mixed with super P and polyvinylidene fluoride (PVDF) with a weight ratio of 6:3:1 in NMP, followed by coating on an Al foil and drying in vacuo at 120 °C overnight. The composite film was then peeled off from the Al foil and cut into discs with a diameter of 15 mm. The discs were pressed onto a stainless-steel mesh to form the final electrode. The electrode thus obtained was used to assemble the coin cell as described above. The cell was cycled at 0.02 C to a certain potential in order to form both α and β phases in the electrode. The cell was then disassembled in the glove box, and the electrode was washed using dimethoxyethane (DME). The XRD measurements were conducted on an X-ray Diffractometer (Rigaku SmartLab 9kW - Advance). The electrode was placed in a vacuum temperature chamber for the temperature-resolved measurements, and the temperature was controlled by liquid N_2 and an electronic heater. The

XRD patterns were collected from 20° to 60° with a speed of 2°/min at 173 K, 300 K, 600 K and 800 K, respectively.

4.5. In situ scanning electrochemical microscopy (SECM)

SECM measurements were carried out using Bio-Logic M470 with a four-electrode open cell made of polytetrafluoroethylene (PTFE). The PTFE cell was filled with electrolyte, and one of the working electrodes containing TiO_2 nanoparticles, PVDF and carbon black was placed at the bottom, with the other working electrode (15 μm Pt microelectrode) sealed in glass as the SECM tip; Li metal was used as reference electrode, and Pt served as a counter electrode. The electrode surface tilt was corrected prior to all measurements. An area scan was performed after the tip was positioned near the surface. Images with an area of 80 μm×80 μm were taken using a step size of 8 μm along both the x-axis and y-axis.

4.6. Synthesis of anatase TiO_2 nanowires

The synthesis method was similar to that reported by Li et al [7]. Typically, 2 g of TiO_2 nanoparticles were dispersed in 80 mL of KOH solution (10 M), and the mixture was heated in a 100-mL Teflon-lined autoclave at 200 °C for 24 h and then cooled to room temperature. The obtained $K_2Ti_6O_{13}$ nanowires were isolated from the solution by centrifugation and washed three times with deionized water. The products underwent ion exchange using a 0.5 M HCl solution by agitating for 4 h and were isolated via centrifugation; this step was repeated three times. The obtained products were washed with deionized water and dried at 60 °C for 12 h. Finally, the products were heat treated at 500 °C in air for 10 h in a high-temperature muffle furnace.

Declaration of competing interest

27

The authors declare that they have no known competing financial interests or personal relationships that could have appeared to influence the work reported in this paper.

Appendix A. Supplementary data

Supplementary data to this article can be found online.

References

[1] Y. M. Chiang, Science 2010, 330, 1485-1486.

[2] M. Armand, J. M. Tarascon, Nature 2008, 451, 652-657.

[3] J. Lee, A. Urban, X. Li, D. Su, G. Hautier, G. Ceder, Science 2014, 343, 519-522.

[4] L. Z. Zhao, H. H. Wu, C. H. Yang, Q. B. Zhang, G. M. Zhong, Z. M. Zheng, H. X. Chen, J. M. Wang, K. He, B. L. Wang, T. Zhu, X. C. Zeng, M. L. Liu, M. S. Wang, Acs Nano 2018, 12, 12597-12611.

[5] C. Y. Wang, G. Zhang, S. Ge, T. Xu, Y. Ji, X. G. Yang, Y. Leng, Nature 2016, 529, 515-518.

[6] A. Varzi, L. Mattarozzi, S. Cattarin, P. Guerriero, S. Passerini, Advanced Energy Materials 2017, 1701706.

[7] K. Li, B. Li, J. Wu, F. Kang, J. K. Kim, T. Y. Zhang, ACS Appl Mater Interfaces 2017, 9, 35917-35926.

[8] E. Markevich, G. Salitra, D. Aurbach, J Electrochem Soc 2016, 163, A2407-A2412.

[9] B. Han, T. Paulauskas, B. Key, C. Peebles, J. S. Park, R. F. Klie, J. T. Vaughey, F. Dogan, ACS Appl Mater Interfaces 2017, 9, 14769-14778.

[10] Q. Li, S. Jiao, L. Luo, M. S. Ding, J. Zheng, S. S. Cartmell, C. M. Wang, K. Xu, J. G. Zhang, W. Xu, ACS Appl Mater Interfaces 2017, 9, 18826-18835.

[11] K. Yamagiwa, D. Morita, N. Yabuuchi, T. Tanaka, M. Fukunishi, T. Taki, H. Watanabe, T. Otsuka, T. Yano, J.-Y. Son, Y.-T. Cui, H. Oji, S. Komaba, Electrochimica Acta 2015, 160, 347-356.

[12] B. W. Yang, H. Zhang, L. Yu, W. Z. Fan, D. H. Huang, Electrochimica Acta 2016, 221, 107-114.

[13] S. S. Zhang, K. Xu, T. R. Jow, Electrochemistry Communications 2002, 4, 928-932.

[14] K. Chen, Z. Yu, S. Deng, Q. Wu, J. Zou, X. Zeng, Journal of Power Sources 2015, 278, 411-419.

[15] C. K. Huang, J. S. Sakamoto, J. Wolfenstine, S. Surampudi, J Electrochem Soc 2000, 147, 2893-2896.

[16] S. T. Guo, S. X. Zhao, K. Bi, Y. F. Deng, K. Xiong, C. W. Nan, Electrochimica Acta 2016, 222, 1733-1740.

[17] N. N. Zhao, Y. S. Li, X. X. Zhao, X. K. Zhi, G. C. Liang, Journal of Alloys and Compounds 2016, 683, 123-132.

[18] D. Lin, K. Li, Q. Wang, L. Lyu, B. Li, L. Zhou, Journal of Materials Chemistry A 2019, 7, 19297.

[19] K. Li, X. Zhou, A. Nie, S. Sun, Y. B. He, W. Ren, B. Li, F. Kang, J. K. Kim, T. Y. Zhang, Nano Lett 2017, 17, 1282-1288.

[20] N. Meethong, H. Y. S. Huang, W. C. Carter, Y. M. Chiang, Electrochem Solid St 2007, 10, A134-A138.

[21] C. Delacourt, P. Poizot, J.-M. Tarascon, C. Masquelier, Nature Materials 2005, 4, 254-260.

[22] M. Y. Yan, G. B. Zhang, Q. L. Wei, X. C. Tian, K. N. Zhao, Q. Y. An, L. Zhou, Y. T. Zhao, C. J. Niu, W. H. Ren, L. He, L. Q. Mai, Nano Energy 2016, 22, 406-413.

[23] G. B. Zhang, T. F. Xiong, M. Y. Yan, Y. N. Xu, W. H. Ren, X. Xu, Q. L. Wei, L. Q. Mai, Chemistry of Materials 2017, 29, 8057-8064.

[24] X. Chen, Y. Tang (Nanyang Technological University) US Patent US20190097210A1, 2019.

[25] M. Wagemaker, G. J. Kearley, A. A. van Well, H. Mutka, F. M. Mulder, Journal of the American Chemical Society 2003, 125, 840-848.

[26] H. Liu, F. C. Strobridge, O. J. Borkiewicz, K. M. Wiaderek, K. W. Chapman, P. J. Chupas, C. P. Grey, Science 2014, 344.

[27] P. Bai, D. A. Cogswell, M. Z. Bazant, Nano Letters 2011, 11, 4890-4896.

[28] Y. H. Kao, M. Tang, N. Meethong, J. M. Bai, W. C. Carter, Y. M. Chiang, Chemistry of Materials 2010, 22, 5845-5855.

[29] N. Sharma, X. W. Guo, G. D. Du, Z. P. Guo, J. Z. Wang, Z. X. Wang, V. K. Peterson, Journal of the American Chemical Society 2012, 134, 7867-7873.

[30] J. Lim, Y. Y. Li, D. H. Alsem, H. So, S. C. Lee, P. Bai, D. A. Cogswell, X. Z. Liu, N. Jin, Y. S. Yu, N. J. Salmon, D. A. Shapiro, M. Z. Bazant, T. Tyliszczak, W. C. Chueh, Science 2016, 353, 566-571.

[31] M. Wagemaker, W. J. H. Borghols, F. M. Mulder, Journal of the American Chemical Society 2007, 129, 4323-4327.

[32] Q. C. Zhuang, J. M. Xu, X. Y. Fan, G. Z. Wei, Q. F. Dong, Y. X. Jiang, L. Huang, S. G. Sun, Sci China Ser B 2007, 50, 776-783.

[33] Q. C. Zhuang, X. Y. Qiu, S. D. Xu, Y. H. Qiang, S. G. Sun, Diagnosis of Electrochemical Impedance Spectroscopy in Lithium-Ion Batteries, InTech, 2012.

[34] Q. C. Zhuang, S. D. Xu, X. Y. Qiu, Y. L. Cui, L. A. Fang, S. G. Sun, Prog Chem 2010, 22, 1044.

[35] J. Y. Song, H. H. Lee, Y. Y. Wang, C. C. Wan, Journal of Power Sources 2002, 111, 255-267.

[36] W. Zhang, F. Ghamouss, A. Darwiche, L. Monconduit, D. Lemordant, R. Dedryvere, H. Martinez, Journal of Power Sources 2014, 268, 645-657.

[37] J. S. Gnanaraj, R. W. Thompson, S. N. Iaconatti, J. F. DiCarlo, K. M. Abraham, Electrochem Solid St 2005, 8, A128-A132.

[38] B. Orvananos, T. R. Ferguson, H. C. Yu, M. Z. Bazant, K. Thornton, Journal of the Electrochemical Society 2014, 161, A535-A546.

[39] T. R. Ferguson, M. Z. Bazant, J Electrochem Soc 2012, 159, A1967-A1985.

[40] C. Delmas, M. Maccario, L. Croguennec, F. Le Cras, F. Weill, Nat Mater 2008, 7, 665-671.

[41] W. C. Chueh, F. El Gabaly, J. D. Sugar, N. C. Bartelt, A. H. McDaniel, K. R. Fenton, K. R. Zavadil, T. Tyliszczak, W. Lai, K. F. McCarty, Nano Letters 2013, 13, 866-872.

[42] W. Dreyer, J. Jamnik, C. Guhlke, R. Huth, J. Moskon, M. Gaberscek, Nature Materials 2010, 9, 448-453.

[43] W. Dreyer, C. Guhlke, R. Huth, Physica D 2011, 240, 1008-1019.

[44] M. Tang, H. Y. Huang, N. Meethong, Y. H. Kao, W. C. Carter, Y. M. Chiang, Chem Mater 2009, 21, 1557-1571.

[45] N. J. J. de Klerk, A. Vasileiadis, R. B. Smith, M. Z. Bazant, M. Wagemaker, Phys Rev Mater 2017, 1.

[46] X. Y. Zhang, M. van Hulzen, D. P. Singh, A. Brownrigg, J. P. Wright, N. H. van Dijk, M. Wagemaker, Nano Letters 2014, 14, 2279-2285.

[47] D. P. Singh, F. M. Mulder, A. M. Abdelkader, M. Wagemaker, Advanced Energy Materials 2013, 3, 572-578.

[48] B. Orvananos, R. Malik, H. C. Yu, A. Abdellahi, C. P. Grey, G. Ceder, K. Thornton, Electrochimica Acta 2014, 137, 245-257.

[49] J. P. Perdew, K. Burke, M. Ernzerhof, *Phys. Rev. Lett.* 1996, *77*, 3865.

[50] H. Huang, H. H. Wu, X. J. Wang, B. L. Huang, T. Y. Zhang, *Phys. Chem. Chem. Phys.* 2018, *20*, 20525-20533.

[51] G. Kresse, J. Furthmuller, *Phys. Rev. B* 1996, *54*, 11169.

[52] G. Kresse, *J. Non-Cryst. Solids* 1995, *193*, 222.

[53] E. Hernandez, *J. Chem. Phys.* 2001, *115*, 10282.

[54] M. Parrinello, A. Rahman, *Phys. Rev. Lett.* 1980, *45*, 1196; M. Parrinello, A. Rahman, *J. Appl. Phys.* 1981, *52*, 7182.

[55] W. Humphrey, A. Dalke, K. Schulten, *J. Mol. Graph. Model* 1996, *14*, 33.

Dr. Kaikai Li obtained his PhD degree from the Hong Kong University of Science and Technology. He joined the School of Materials Science and Engineering, Harbin Institute of Technology (Shenzhen) as an Assistant Professor in 2020. His current research interest is to develop fundamental understanding of electrochemical energy storage processes in Li-ion batteries and Na-ion batteries and develop new battery materials.

Dongmei Lin obtained her master degree from Beijing University of Chemical Technology in 2017. She is currently a third PhD candidate of The Hong Kong Polytechnic University. Her research interests mainly focus on exploring the effect of temperature on the inherent reaction mechanism and phase transition of LIBs and SIBs electrodes, and improving the storage performance of batteries at low temperatures.

He Huang received his B.S. degree from the Department of Aerospace at Xi'an Jiaotong University in 2014 and Ph.D. degree in Mechanical and Aerospace Engineering from the Hong Kong University of Science and Technology in 2019. He is currently a postdoctoral research fellow in Professor Baoling Huang's research group. His current research interests include

theoretical studies of alkali-ion transport mechanism and improvement in energy storage materials.

Prof. Tong-Yi Zhang is the Dean of Shanghai University Materials Genome Institute. He joined the School of Materials Science and Engineering, Harbin Institute of Technology (Shenzhen) in 2020. His research interests are mechanical properties of materials, surface stress and surface energy of solids, defects of crystals, fracture of piezoelectric materials, diffusion and phase transformation, and micro/nanomechanics of materials.

Prof. Limin Zhou received his PhD degree from The University of Sydney in 1994. He was appointed as an Assistant Professor in 1996 and became a Professor in 2005 in the Department of Mechanical Engineering, The Hong Kong Polytechnic University. In 2019, Prof. Zhou joined the School of System Design and Intelligent Manufacturing at Southern University of Science and Technology as a Chair Professor. Prof. Zhou's major research interests include advanced composite materials and structures, smart materials and structures, nanomaterials and nanotechnology for energy storage and conversions, and structural health monitoring techniques.